AFRL-RZ-WP-TR-2010-2155

NONEQUILIBRIUM PLASMA RESEARCH

Biswa N. Ganguly

Energy and Power Systems Branch
Energy/Power/Thermal Division

MAY 2010
Final Report

Approved for public release; distribution unlimited.

See additional restrictions described on inside pages

STINFO COPY

AIR FORCE RESEARCH LABORATORY
PROPULSION DIRECTORATE
WRIGHT-PATTERSON AIR FORCE BASE, OH 45433-7251
AIR FORCE MATERIEL COMMAND
UNITED STATES AIR FORCE

NOTICE AND SIGNATURE PAGE

AFRL-RZ-WP-TR-2010-2155 HAS BEEN REVIEWED AND IS APPROVED FOR PUBLICATION IN ACCORDANCE WITH THE ASSIGNED DISTRIBUTION STATEMENT.

*//Signature//

BISWA N. GANGULY
Program Manager
Thermal and Electrochemical Branch
Energy/Power/Thermal Division

//Signature//

JOSEPH W. WEIMER, Branch Chief
Energy and Power Systems Branch
Energy/Power/Thermal Division
Propulsion Directorate

This report is published in the interest of scientific and technical information exchange, and its publication does not constitute the Government's approval or disapproval of its ideas or findings.

*Disseminated copies will show "//Signature//" stamped or typed above the signature blocks.

REPORT DOCUMENTATION PAGE

Form Approved
OMB No. 0704-0188

1. REPORT DATE *(DD-MM-YY)*	2. REPORT TYPE	3. DATES COVERED *(From - To)*
May 2010	Final	02 January 2004 – 31 December 2009

4. TITLE AND SUBTITLE
NONEQUILIBRIUM PLASMA RESEARCH

5a. CONTRACT NUMBER
In-house

5b. GRANT NUMBER

5c. PROGRAM ELEMENT NUMBER
61102F

6. AUTHOR(S)
Biswa N. Ganguly

5d. PROJECT NUMBER
2301

5e. TASK NUMBER
29

5f. WORK UNIT NUMBER
23012900

7. PERFORMING ORGANIZATION NAME(S) AND ADDRESS(ES)
Energy and Power Systems Branch (AFRL/RZPE)
Energy/Power/Thermal Division
Air Force Research Laboratory, Propulsion Directorate
Wright-Patterson Air Force Base, OH 45433-7251
Air Force Materiel Command, United States Air Force

8. PERFORMING ORGANIZATION REPORT NUMBER
AFRL-RZ-WP-TR-2010-2155

9. SPONSORING/MONITORING AGENCY NAME(S) AND ADDRESS(ES)
Air Force Research Laboratory
Propulsion Directorate
Wright-Patterson Air Force Base, OH 45433-7251
Air Force Materiel Command
United States Air Force

10. SPONSORING/MONITORING AGENCY ACRONYM(S)
AFRL/RZPE

11. SPONSORING/MONITORING AGENCY REPORT NUMBER(S)
AFRL-RZ-WP-TR-2010-2155

12. DISTRIBUTION/AVAILABILITY STATEMENT
Approved for public release; distribution unlimited.

13. SUPPLEMENTARY NOTES
PAO Case Number: 88ABW-2010-3013, Clearance Date: 03 Jun 2010. Report contains color.

14. ABSTRACT
We report novel measurement techniques and also validate other methods which permit to make absolute quantitative measurement of gas temperature, radical density, UV intensities, plasma power deposition efficiency, sheath electric field, ionic and neutral species formed by electron and photon energy transfer to the medium. The quantitative measurements include hair pin resonator for electron density, diode laser absorption for metastable line density, two-photon laser induced fluorescence (LIF) for atom density measurement, and mass spectrometric measurements.

15. SUBJECT TERMS
Plasma physics and magneto-hydrodynamics, Optical and Microwave measurements

16. SECURITY CLASSIFICATION OF:			17. LIMITATION OF ABSTRACT:	18. NUMBER OF PAGES	19a. NAME OF RESPONSIBLE PERSON (Monitor)
a. REPORT	b. ABSTRACT	c. THIS PAGE			Biswa N. Ganguly
Unclassified	Unclassified	Unclassified	SAR	46	19b. TELEPHONE NUMBER *(Include Area Code)* N/A

Standard Form 298 (Rev. 8-98)
Prescribed by ANSI Std. Z39-18

Table of Contents

Lists of Figures

List of Tables

Preface

This technical report contains part of the work completed under the in–house project work unit 23012900, titled “Nonequilibrium Plasma Research”. The project engineer for this task is Dr. Biswa N. Ganguly. The research for this work was performed in the period 02 January, 2004 through 31 December, 2009.

1. Introduction

We have investigated the energy coupling mechanisms of rapidly varying (temporal and/or spatial) electrostatic and electromagnetic fields with the bound and free electrons which, in turn, would selectively deposit energy in gaseous medium with and without the presence of nano and micro clusters. The experimentally generated nonequilibrium plasma are characterized by, at minimum, a nonMaxwellian electron energy distribution (and electron mean energy much greater than the heavy particle energy) which are be in equilibrium with the local reduced electric fields, and at the other extreme conditions the local electron energy deposition rate could be out of phase (spatially and/or temporally) with the reduced electric field. One would expect to produce the later type of plasma by very short pulse duration high peak power laser or other types of Electro-static (ES) or Electro-magnetic (EM) pulsed fields. In the laboratory, we have produce this type of plasma by short pulse excited dielectric barrier discharge], ionization wave excited plasmas, or micro-streamer generated plasma. These experiments allowed us to investigate the efficiency of these types of discharges for the production of reactive atoms, radicals, Ultra-violet (UV)-Vacuum Ultra-violet (VUV) light source, surface property modifications of temperature sensitive materials, and toxic material remediation, supersonic/high altitude combustion and ignition augementation. In these types of discharges, nonequilibrium properties arise from the rate of ES or EM energy input versus the collisional redistribution of electron energies with the heavy particles.

The ability to determine the efficiency and the scalability of controlled energy deposition by highly nonequilibrium plasma for VUV-UV, and radical flux generation, ignition and combustion enhancement, shock wave mitigation, etc. require quantitative measurements of the parameters which usually show nonlinear dependence on both spatial and/or temporal variation E/n. Under this in-house task we have develop novel measurement techniques and also validate other methods which permit to make absolute quantitative measurement of gas temperature, radical density, UV intensities, plasma power deposition efficiency, sheath electric field, ionic and neutral species formed by *electron and photon energy* transfer to the medium. Quantitative measurements are crucial for understanding scaling properties and concept transition to a product development. The quantitative measurements include hair pin resonator for electron density, diode laser absorption for metastable line density, two-photon laser induced fluorescence (LIF) for atom density measurement, and mass spectrometric measurements.

The detail measurement of atomic hydrogen production efficiency in a short pulse high voltage methane discharge by two-photon LIF is described in section 2, and hairpin resonator measurement of electron density is described in section 3. In section 4 the effects of voltage pulse rise time on the production efficiency of argon metastable is reported as a function of gas pressure up to 500 Torr using diode laser absorption spectroscopy. Mass spectrometric measurement of JP-10 dissociation in a rf plasma is described in section 5. A novel concept of the formation of an atmospheric pressure plasma jet is described in section 6. The list of publications is given in section 7. Some of the research was conducted jointly with Professor Tachibana's group at Kyoto University, Japan and it was funded through Asian Office of Aerospace Research &development (AOARD). The research work was conducted at both Kyoto University, at on-site AFRL research facilities and at CAPEC lab at Wright State University.

One of the more recent results was published as a technical report, TR# AFRL-RZ-WP-TP-2010-2025 (AD number A51614).

2. Streamer Evolution in a Methane-Based Pulsed-DC Discharge

Methane-based discharges hold high promise in applications ranging from thin film deposition to combustion initiation.[1,2] Efficient dissociation of methane via direct electron impact is realized through (5-mm gap) pulsed-dc discharges that rapidly (<20 ns) achieve an overvoltage condition before breakdown. Current and voltage measurements reveal a quasi steady-state discharge condition for 100 ns or more following breakdown. At low pressure (<30 Torr), the plasma appears as a homogenous volume discharge. For pressures near 100 Torr the appearance changes to a streamer-dominated one.

The measurements reported here were made using parallel plate electrodes one cm in diameter spaced one-half cm apart. The electrodes were enclosed in a pyrex chamber fitted with planar quartz windows to permit optical measurements. A 15-ns-rise-time high-voltage stacked MOSFET switch was used to apply 6 kV to the electrodes for pulse durations of 250 ns at a 100-Hz repetition rate. Overvoltage conditions were achieved in less than 20 ns. After breakdown the voltage and current settle into steady-state values of 1.5 kV and 15 A that last for 140 ns before dropping as the switch opens. The total pressure and total gas flow rate were controlled at 100 Torr and 20 sccm, respectively. A 20/80 mixture of methane and nitrogen was used. Low-resolution emission spectra of the discharge indicate N_2 C-B bands, CN* and C_2* bands, along with spectral features of the direct electron impact dissociation fragments H* and CH*. Single-shot and averaged images of the streamers were recorded using an intensified CCD camera. The camera gate was set to 20 ns and delayed with respect to the overvoltage peak by 20-ns intervals beginning at the peak. An interference filter with a 10-nm bandwidth centered at 431 nm was placed in front of the ICCD camera. The filter transmitted emission from the A-X band of CH*. Spectrally-resolved CH (A-X) emission indicates radiation from both the 0-0 and 2-2 vibration bands. The rotational temperature is on the order of 800 – 1200 K, and the vibrational distribution appeared non-Boltzmann while the translation temperature of the bulk gas is less than 500 K.

The single-shot images are characterized by the appearance of a single steamer at both early and long delays. The overall intensity of the single streamers at a fixed delay varies somewhat while their widths do not. During steady-state, the single-shot images reveal one or two streamers. Images averaged for one second (100 shots) show as many as 8 individual streamers with little or no overlap between them. While the intensity of individual streamers can vary at a fixed delay, the overall trend is for the mean streamer intensity to increase from the overvoltage peak to the midpoint of the steady-state condition and then to fall again for increasing delay. Figure 1 shows a sequence of four averaged (100 shots) spectrally-filtered CH* images acquired 40 ns apart beginning 20 ns after the overvoltage. The images are two-dimensional projections of the discharge volume between the plate electrodes. The projection lies in the x-y plane of the images with the emission intensity appearing in the z direction. The dashed red line parallel to the x-axis in the first image indicates the location and spatial extent of the cathode and the anode is similarly identified by the solid red line. Each of the other three images has the identical orientation and spatial scaling as the first image. Since these images are two-dimensional projections they mask the fact that the streamers form predominantly near the edges of the electrodes. At a delay of 0 ns, the CH* emission is most intense near the cathode where the local E/p value peaks. At longer delays the intensity distribution becomes more uniform throughout the inter-electrode volume in each streamer channel although the peak intensity is always localized near the cathode. Images taken for delays greater than 180 ns reflect

the current fall and only faint emission is seen near the cathode surface. The images at delays of 100 and 140 ns lie well within the steady-state current/voltage condition. The width of the streamer channels increases in time due to electron avalanche growth and at high current due to the self-consistent space-charge electric field growth. At 20 ns the brightest channel has a width of ~1 mm. The characteristic channel width more than doubles by 100 ns.

In brief, these measurements indicate that high-pressure overvoltage conditions in methane/nitrogen mixtures lead to streamer formation; hence, radical production is spatially localized to some extent.

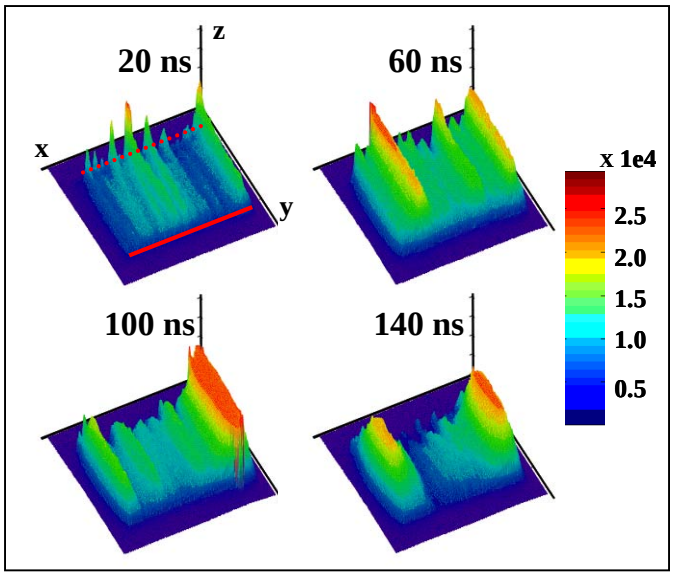

Figure.1 Spectrally-filtered CH* Emission Images of Streamer Evolution in a 100-Torr, Methane/Nitrogen, Pulsed-dc Discharge as a Function of Delay from Breakdown

3. Absolute H Atom Density Measurement in Short Pulse Methane Discharge.

3A. Introduction

In supersonic combustion (scramjet) systems the flow speed is very high so that mixing and reaction times are limited [3-5]. Some flow conditions also give rise to very low mixture temperatures [3]. For either condition, additional sources of ignition or combustion enhancement are needed. Plasma torch ignitors [3, 4] have been investigated widely, and microwave discharges [5] have been studied, as means of providing reliable scramjet combustion. However, such approaches require multi-kilowatt electrical power inputs and are not easily volume scaleable. Highly nonequilibrium plasma production of energetic reactive hydrocarbon fragments could have application in situations where more conventional means of promoting and sustaining combustion are degraded [6]. The attractiveness of high E/n, where E is the electric field and n is the gas density, for fostering dissociation, electronic excitation and ionization is clear from both theoretical [7, 8] and experimental [9] work performed on corona and dielectric barrier discharges.

Pulsed dc discharges in gaseous hydrocarbon mixtures can provide substantial amounts of atomic hydrogen, as well as electronically excited hydrocarbon fragment neutrals and ions. Such discharge products would be useful in promoting combustion in a wide variety of fuel to air mixtures. Additionally, control of discharge parameters offers the possibility of varying the yields of the dominant reaction products in response to changing conditions in an application. The volume and energy scaling of highly nonequilibrium plasma assisted ignition could improve overall efficiency of supersonic combustion. It is, therefore, important to quantify the radical production efficiency of a plasma device which could be used to replace a conventional spark ignition module. We have developed a short pulse excited discharge device [10] which can operate at high reduced electric field (E/n) with PD, P is the gas pressure and D is the gap distance, scaling up to 50 Torr.cm. Actinometric and plasma induced emission measurements performed in this high reduced electric field plasma device indicated that the CH_4 dissociation efficiency can be more than an order of magnitude greater than thermal dissociation process. Although those measurements gave indications that a short pulse discharge can produce radicals with higher efficiency, compared to the thermal dissociation, absolute measurement accuracy of those techniques is limited by the applicability of the actinometeric technique. In this paper we report absolute H atom ground state density measurements in a short pulse methane discharge by two-photon allowed LIF (TALIF) technique. The H atom TALIF intensity has been calibrated by comparing TALIF intensity from Kr atom ground state [9] to obtain absolute H atom density.
The goals of this study are: 1) construct a high E/n discharge system capable of producing discharges over a substantial range of input energy density, and 2) conduct spectroscopic measurements of the absolute H-atom production to estimate plasma dissociation efficiency of CH_4 in high E/n discharges. Pulsed gas discharges in CH_4 produce all possible methane fragments (CH_3, CH_2, CH, C and H) and their ions in varying ratios depending upon the discharge E/n. In previous work [10], we have quantified the direct electron impact dissociation efficiency of CH_4 by actinometric measurement of H_α emission by comparing it to a pure hydrogen reference discharge. In the present study, we provide an accurate estimate of the direct electron impact dissociation efficiency of CH_4 in short pulse excited, high E/n discharge, with more than an order of magnitude higher energy density, using absolute H atom number density

measurement by calibration of H atom TALIF signal with near isoenergetic Kr ground state atom TALIF measurement [11].

3B. Experimental approach.

A solid-state, high-voltage, high-speed switch (15 kV, 30 A) provided a fast rise time voltage pulse and was controlled by timing control electronics. As shown in Figure 2, the voltage pulse was delivered (rise time <15 ns) via a microstrip transmission line to an end-fed coaxial section.

Again in figure 2, four quartz windows W provided optical access. The discharge gap was viewed by a gated photomultiplier tube (PMT) fitted with an optical relay lens TL and preceded by F a long pass and a neutral density filter. The gated PMT allow photon detection after the plasma drive voltage was turned off and the plasma emission had decayed. The laser was fired 250 ns after the voltage pulse was turned off. The pulse discharge and the TALIF data acquisition timing was controlled by a delay generator pulser and t=0 on all the data plots correspond to the start of the voltage pulse.

The 615 nm pulsed dye laser output tripled by a combination of KDP and BBO crystals and the TALIF emission was measured with a gated PMT. The optical path, including attenuation and collection solid angle, was kept fixed for all measurements. The laser beam was focused near the middle of the discharge volume and it was located 2 mm below the cathode surface for optimum TALIF signal. Absolute calibration used successive measurements of TALIF signals at two wavelengths; 205.08 nm probed the ground state of hydrogen atom produced by the pulsed discharge in methane and the 204.13 nm TALIF measured the calibration signal from the ground state of krypton atom.[9] These two probe wavelengths are close enough to ensure the input optics spectral throughput parameters remain constant. The 205.08 nm wavelength two-photon excites population of hydrogen atoms from the ground state, 1s, to 3d and 3s levels. The TALIF signal is detected by photon emission at 656.3 nm (H_α). The other probe wavelength excites a krypton transition from the ground state, $4p^6$, to 5p´ levels, using two photons at 204.13 nm and the emission from 5p´ to 5s´ was detected at 826.3 nm. For ease of calibration the two TALIF signal were set approximately equal amplitude by adjusting the pressure of Kr. A pyroelectric detector measurement was conducted at the beginning and end of a series of TALIF measurements to assure that probe laser energy had not changed.

All the measurements have been performed in pure CH_4 discharge at 20 Torr pressure with 5 mm gap between the 1 cm diameter electrodes. The applied voltage was varied from 4 kV up to 6 kV with 480 ns pulse duration. Gas flow and pressure was controlled by a mass flow controller loop using a exhaust valve controller and a mass flow readout, and Baratron pressure transducer. Throughout this study the gas flow rate was fixed at 30 SCCM. The CH_4 gas was UHP grade (99.999%).

3C. Experimental results and discussions

The pulsed discharge voltage, current and power deposited in the discharge are shown in figures 3, 4 and 5, respectively. The discharge voltage measurement of high speed pulses (<15 ns) show the gap voltage initially spikes, due to pre breakdown over volting, to a high value. At 6 kV applied voltage, the 20 Torr pure methane discharge runs at current density, j, up to 25

Amp/cm^2. Assuming j/P^2 scaling of the cathode sheath voltage drop [12] for pure methane discharge is similar to that of H_2 discharge; the cathode fall voltage can be 700-750 volts for these conditions. About 20 to 50 ns after breakdown, depending on drive voltage, a lower plateau gap voltage and the discharge impedance is established for the measured 480 ns voltage pulse duration. The discharge operating voltage is dependent on the initial applied voltage; it varies from 1100 volts at 6 kV down to 900 volts at 4 kV. The corresponding volume average discharge E/n can vary from 60 Td to 120 Td (1Td = 10^{-17} Volt cm^{-2}). The peak E/n can exceed 300 Td. Pressure dependent krypton TALIF calibration signal were measured and was found to be linear with pressure. Calibration transfer was made via a measurement at 0.318 Torr, where Kr signal amplitude was comparable to the H atom TALIF. A representative set of this series is shown in figure 6 for three pressures 0.218, 0.387, and 0.513 Torr. Immediately following the Kr atom TALIF measurement, ground state H atom production in CH_4 discharge was measured.
The H atom TALIF intensity has been calibrated by comparing TALIF intensity from Kr atom ground state to obtain absolute H atom density using the equation given below.

$$n_H = \kappa \frac{a_{23}(Kr)}{a_{23}(H)} \frac{\sigma^{(2)}(Kr)}{\sigma^{(2)}(H)} \frac{S_{PMT}(H)}{S_{PMT}(Kr)} \left(\frac{I_L(Kr)}{I_L(H)} \right)^2 n_{Kr} \qquad (1)$$

where n_H and n_{Kr} are the absolute number density of the H- and Kr-atoms respectively, κ is a transmission and sensitivity factor for the optical set-up and detector at the two wavelengths, a_{23} is the optical branching ratio ($a_{23} = A_{23} / \Sigma A_{2i}$, A_{23} is the spontaneous emission coefficient and ΣA_{2i} is the sum of spontaneous emission and collisional quenching coefficients), $\sigma^{(2)}$ is the two-photon cross section, S_{PMT} is the measured TALIF signal, and I_L is the intensity of the laser radiation. The ratio of the two-photon cross-sections, Kr atom optical branching ratio and collisional quenching rate of H atom 3d and 3s states by CH_4 are given in reference 11. Under our measurement conditions, the value of κ depends on the ratio of the PMT response sensitivity at 656.3 nm and 826.3 nm, which is obtained from the manufacturer's data sheet. Thus from a measurement of both the H-atom and Kr-atom TALIF signals, the absolute number density of H-atoms can be calibrated with a known number density of ground state Kr atom. Figure 6 shows H atom TALIF signals, calibrated in absolute number density, obtained with three different applied drive voltages from 4 kV to 6 kV, with 480 ns pulse duration. The total input energy for these discharges were 6.5, 8.7, 11.4 mJ, respectively. For the corresponding discharge conditions, the measured H atom density ranged from ~ 9.8×10^{15} per cm^3 at 4 kV to 2.2×10^{16} per cm^3 at 6 kV (TALIF pulse peak-to-area ratio is essentially constant so the peak values are used), i.e., up to 4% of CH_4 was dissociated at 6 kV applied voltage across the 5 mm gap discharge. Based on the energy deposited near the cathode surface, an estimate of the direct electron impact dissociation efficiency of $CH_4 + e \rightarrow CH_3 + H + e$ can be obtained from the measured H atom yield in this pulsed discharge. The product of the direct electron impact dissociation rate coefficient and electron density in plasma is proportional to the fraction of discharge energy deposited to that process multiplied by the energy deposited in the gas, i.e.:

$$k_{ei}^{CH4} n_e^{CH4} \propto Y(E/n)\, P_{CH4} \qquad (2)$$

where $Y(E/n)$ is the fractional energy deposited into electron impact production of CH_3+H(n=1) as a function of E/n in methane discharges, k_{ei}^{CH4} is the electron impact dissociation rate, n_e^{CH4} is the electron density, and P_{CH4} is total discharge energy. Note that 70 to 75% of the energy is deposited in the discharge volume within 2 mm from the cathode surface. For the 6 kV applied voltage discharge with 11.4 mJ total discharge energy, this would

correspond to the discharge energy density ~ 70 mJ/cm^3. Assuming an average CH_4 dissociation energy cost of 10 eV, the total energy required to produce H atom density of 2.2×10^{16} per cm^3 would be 35 mJ/cm^3 (direct electron impact dissociation threshold [13] of $CH_4 + e \rightarrow CH_3 + H + e$ is 8.5 eV, and at the threshold energy the dissociation rate is very small. The higher dissociation rate, k_{ei}^{CH4}, with average electron energy cost of 10 eV would be more appropriate for this short pulse discharge). This would imply about 50% efficiency of the direct electron dissociation of CH_4 in this 6 kV short pulse discharge. Similarly for the 4 and 5 kV discharges, the corresponding energy densities are ~ 40 and 53 mJ/cm^3, respectively. The energy required to produce 9.8×10^{15} per cm^3 H atom density, at 4 kV, would be 15.7 mJ/cm^3 and the CH_4 dissociation efficiency is ~ 40%. For the 5 kV discharge, the energy required to produce H atom density of 1.44×10^{16} per cm^3 would be 23 mJ/cm^3 and the dissociation efficiency is nearly the same as the 4 kV discharge. The measurable difference in the CH_4 dissociation efficiency with the over volting may be caused by the combination of both higher peak power deposition at higher E/n and also the increase in the nonuniformity of the discharge energy deposition across the gap. Although the importance of initial energy deposition near the breakdown under higher E/n cannot be directly quantified from these measurements, they clearly show the advantage of operation at higher applied voltage even for a relatively long pulse duration discharge compared to the initial high peak power pulse duration. In summary, we have used absolute H atom density measurements by TALIF to demonstrate high efficiency operation of over volted short pulse excited discharge for CH_4 dissociation, H atom and CH_3 radical production which can be used for ignition and combustion enhancement for high speed propulsion.

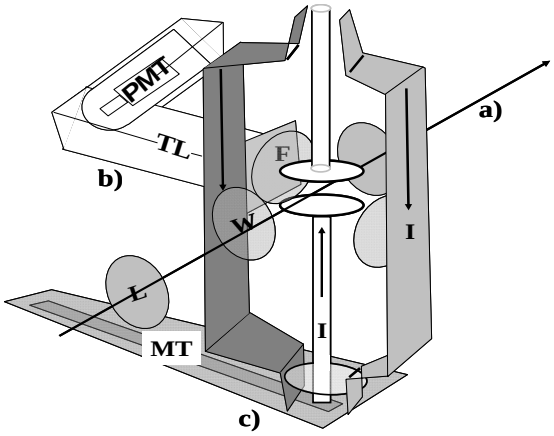

Figure 2. An Experimental Schematic

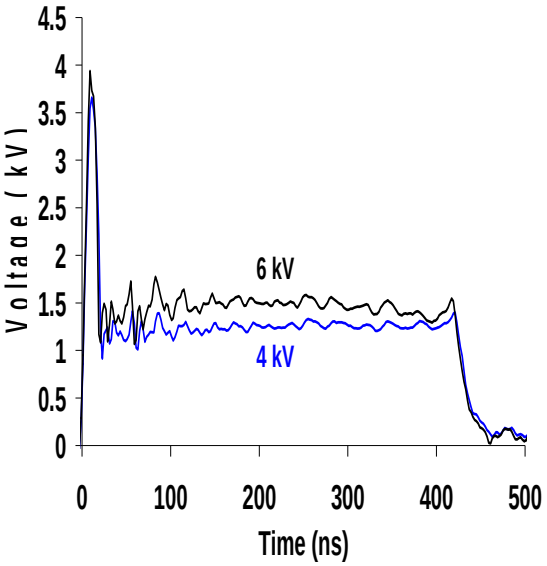

Figure 3**.** Discharge Gap Voltage Pulses for 4 and 6 kV Applied Voltage

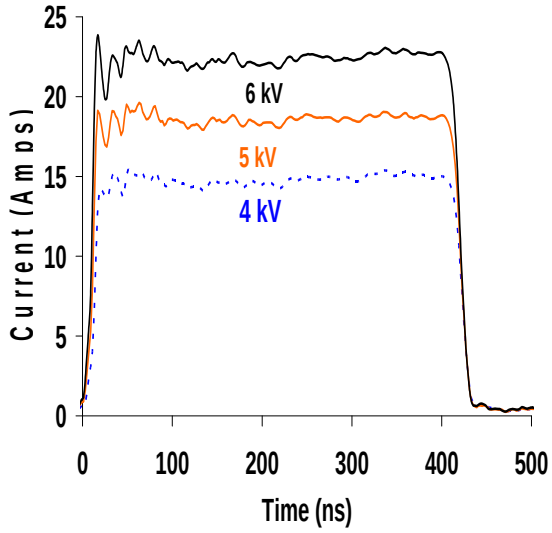

Figure 4. Discharge Current Pulses for 4, 5, and 6 kV Applied Voltages

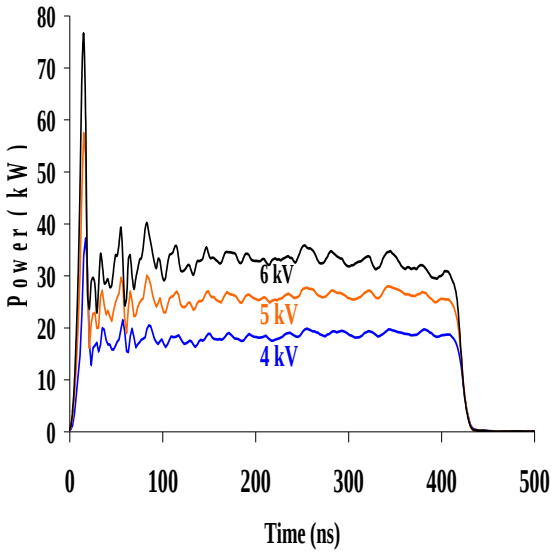

Figure 5. Calculated Power Deposited in the Discharge for the Three Different Applied Voltages

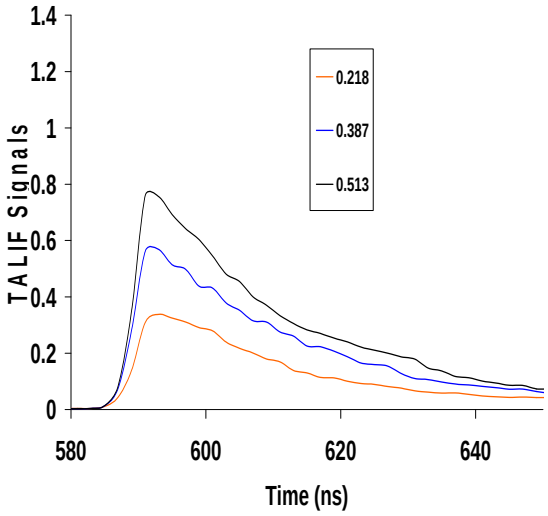

Figure 6. Kr Atom Calibration TALIF Measurements for Gas Pressures 0.218, 0.387, 0.513 Torr

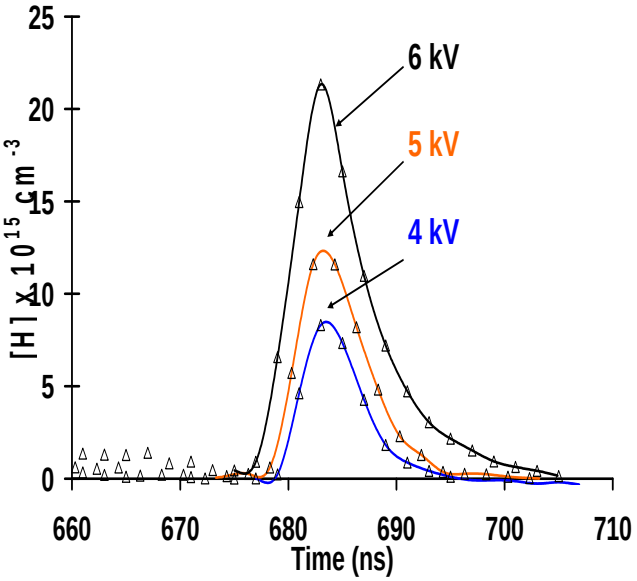

Figure 7. TALIF Measurements of Absolute H Atom Density

4. Decay of the electron number density in the nitrogen afterglow using a hairpin resonator probe

4A. Introduction

Since Stenzel [14] introduced the hairpin resonator in 1976, this diagnostic tool has been used by Hebner et al. [15], Piejak et al. [16,17] and Haas et al. [18] to measure the electron number density in low pressure RF discharges (10 mTorr < p < 300 mTorr). The hairpin resonator is just one of a wide range of available microwave diagnostics for measuring electron number density [19-22]. This paper only briefly describes the theory and experimental set up of the hairpin resonator for measuring the steady-state electron number density since more detailed information can be found in the previously referenced papers [14-18]. The three main goals of this research are to extend the operating pressure range of the hairpin, to convert it into a time-dependent diagnostic tool, and to measure indirectly the electron temperature in the nitrogen afterglow. The focus of this introduction is to address the first research goal by describing hairpin characteristics, the collisional correction and the sheath correction. We address the second goal in the Experimental Results section and the third goal in the Analysis section.

a. Hairpin Characteristics

Figure 8 shows a diagram of the hairpin resonator system. The hairpin consists of a U-shaped piece of 0.5 mm diameter gold wire. The length of the hairpin is 24 mm and the width is 5 mm. Gold wire was chosen for its relatively large conductance. Epoxy holds the loop wire and the hairpin together without allowing a direct electrical connection. The oscillating currents from the sweep generator create oscillating magnetic fields in the loop wire. The oscillating magnetic fields couple to the hairpin when the frequency from the sweep generator is near the quarter-wavelength resonance. At resonance, the hairpin becomes an antenna. A crystal detector, at the end of a waveguide outside of the discharge volume, measures the microwave power radiated by the hairpin.

When we vary the frequency of the microwave sweep generator near the hairpin's resonance, the signal from the crystal detector displays an extremum. This defines the peak frequency, referred to as f_{res}. The quality factor, Q, of the hairpin resonator is the ratio of the peak frequency to the full-width at half-maximum. With no plasma, the Q of our hairpin resonator was 120. With the discharge turned on, the Q of our hairpin resonator was between 120 and 110, depending on pressure and current. The response time of the hairpin resonator to a change in the dielectric constant of the medium is defined as Q / f_{res}. For a resonant frequency of 3 GHz, the rise time of the hairpin is 50 ns. Experimentally, the rise time was 100 ns, due to the RC time constant of the circuit. This response time is more than acceptable for measuring the decay of the electron number density in the afterglow via ambipolar drift to the wall. For example, at pressures near 0.5 Torr and for a tube radius of 1.5 cm, the decay time is on the order of a few hundred microseconds.

The peak resonant frequency of the hairpin [16] is

$$f_{resonant} = c \big/ 4L\sqrt{\varepsilon} \quad , \tag{3}$$

where c is the speed of light in a vaccum, L is the length of the hairpin, and ε is the dielectric constant of the medium between the hairpin wires. The dielectric constant in a collisionless plasma can be expressed as

$$\varepsilon = 1 - \frac{\omega_p^{\,2}}{\omega^2} \quad , \tag{4}$$

where ω_p is the electron plasma frequency, such that $\omega_p^{\,2} = \frac{4\pi e^2 n_e}{m_e}$, and ω is the microwave frequency in rad/s. By analyzing the case of sheaths formed around the hairpin wire, Piejak et al. [16] expressed the electron number density as

$$n_e = \frac{f_{res}^{\,2} - f_0^{\,2}}{0.81 \cdot C_{sheath}} \quad , \tag{5}$$

where f_{res} is the resonant frequency with the plasma on and f_o is the resonant frequency with the plasma off. The unit for the frequencies is GHz and the unit for n_e is 10^{10} cm^{-3}. Piejak et al. [16] calculated the sheath correction factor, C_{sheath}, for the case of a collisionless sheath. C_{sheath} is a function of both the width of the hairpin and the electron Debye length.

The hairpin resonator measures a weighted average of the dielectric constant of the medium between the hairpin wires because the amplitude of the oscillating electric field between the wires increases towards the open end of the hairpin. The electron number density is not uniform in the radial direction of the positive column. The electron number density decreases from the center line to the wall according to a zeroth-order Bessel's function. Therefore, the hairpin resonator measures a spatially-averaged electron number density with the centerline density being weighted the greatest.

b. Collisional Correction

One goal of this research was to operate the hairpin resonator at pressures near 1 Torr. The dielectric constant given in Eq. (4) does not hold when the collision frequency is comparable to or greater than the driving frequency. This is due to the fact that the dielectric constant is no longer strictly real, but rather a complex number dependent on the collision frequency [21],

$$\varepsilon = 1 - \frac{\omega_p^{\,2}}{\omega(\omega - i\upsilon_{en})} \quad , \tag{6}$$

where v_{en} is the electron-neutral momentum-transfer collision frequency. Eq. (4) can be derived assuming that either the electron-neutral collision frequency is independent of velocity or the electron thermal velocity is large compared to the "ordered component" [21]. The ordered component is the velocity the electron gains in the hairpin's oscillating electric field. In nitrogen glow discharges, the collision frequency is strongly dependent on velocity, and the velocity is non-Maxwellian [23]. Therefore, we can not assume that the collision frequency is independent

of velocity. However, we kept the ordered component of the velocity small compared to the electron thermal velocity by keeping the power to the hairpin resonator much lower than the power to the discharge. In which case, Eq. (6) is valid.

We begin by examining the influence of electron-neutral collisions on the peak resonant frequency. The real part of the square root of the dielectric constant, i.e. the dispersion, is displayed in figure 9 as a function of ω_p/ω and ν_{en}/ω for the range of values of interest in a glow discharge. We plot $\varepsilon^{1/2}$ instead of ε because Eq. (3) depends on $\varepsilon^{1/2}$ rather than ε. We plot for values of ω_p/ω less than 0.3 because, as seen in Table I, ω_p/ω does not exceed 0.13 under our discharge conditions. In this range, $\mathrm{Re}(\varepsilon^{1/2})$ is well represented by an equation that is parabolic with respect to ω_p/ω. The best-fit for the real part of the square root of the dielectric constant is

$$\mathrm{Re}\left(\sqrt{\varepsilon}\right) = 1 - \frac{C_{collisional}}{2}\frac{\omega_p^{\,2}}{\omega^2} \quad where \quad C_{collisional} = \frac{1}{1+\left(\nu_{en}/\omega\right)^2} \qquad . \tag{7}$$

The factor of ½ comes from the fact that, for small values of x, $(1 - x)^{1/2} \approx 1 - \frac{1}{2} x$, where $x = (\omega_p/\omega)^{1/2}$. Therefore, the real portion of the dielectric constant is

$$\mathrm{Re}(\varepsilon) = 1 - C_{collisional} \cdot \frac{\omega_p^{\,2}}{\omega^2} \qquad . \tag{8}$$

Figure 10 shows the collision correction factor ($C_{collisional}$) as a function of normalized collision frequency, ν_{en}/ω. The collision correction factor is only a function of ν_{en}/ω. As seen in Figure 10, the collision correction factor is 0.97 when the collision frequency is one fifth of the driving frequency. The electron-neutral momentum-transfer collision frequency in the active discharge is approximated by Raizer [24] to be $\nu_{en}/p = 4.2 \cdot 10^9$ s^{-1} Torr^{-1}. At 0.75 Torr, the normalized collision frequency is 0.15. At 0.25 Torr, the normalized collision frequency is 0.05. The collision correction factor is 0.97 at 0.75 Torr and 0.99 at 0.25 Torr. In the afterglow, the electron-neutral collision frequency decreases, bringing the collision correction factor to 0.98 at 0.75 Torr and 1.00 at 0.25 Torr. The collision correction factor at these pressures is negligible.

c. Sheath Correction

The greatest source of error for the hairpin resonator is determining the magnitude of the sheath correction factor. The sheath correction factor is different in a collisional sheath than in a collisionless sheath. In the case of a collisional sheath around a floating wire [25], the sheath length can be approximated as one electron Debye length. Without a sheath correction factor, Eq. (5) would underestimate the electron number density because, approximately, there are no electrons within one Debye length around the metal wire. For this reason, the Debye length must be smaller than the half-width of the probe. Treating the hairpin as a series LRC-circuit (with two dielectrics of varying thickness in the capacitive element), the sheath correction factor is

$$C_{sheath} = 1 - \frac{\lambda_{Debye}}{h} \qquad , \tag{9}$$

where *h* is half the width of the hairpin. The sheath correction factor, Eq. (9), is plugged into Eq. (5) when computing the electron number densities. This process is iterative because the electron number density in Eq.(5) depends on the Debye length and the Debye length depends on electron number density. The sheath correction factor is listed in Table I at the two pressures and the two currents discussed in the Experimental Results section. As seen in Table I, the sheath correction is more significant at 0.25 Torr than at 0.75 Torr because the electron Debye length is larger at 0.25 Torr than at 0.75 Torr. Within one microsecond in the afterglow, the electron temperature decreases, which causes the electron Debye length and the sheath thickness to decrease compared to their values in the active discharge.

4 B. Experimental set up

The hairpin resonator was placed along the radial direction of the positive column in a DC glow discharge. figure 11 shows a schematic of the experiment. Two conformal wall electrodes, spaced 30 cm apart, create the glow discharge inside of a 3 cm diameter glass tube. Nitrogen gas is flowed through the system with a 40 cm/min flow velocity. In order to shield the sweep generator from both the high voltage floating potential and reflected power, two levels of electrical protection were used. First, there was a microwave isolator that kept the reflected power from going back into the sweep generator. The isolator sent the reflected power to a load resistor when the frequency of the sweep generator did not match the resonance of the hairpin. There was also a high voltage DC block to prevent the floating potential of the hairpin from being transferred to the sweep generator. The floating potential of the hairpin resonator was around 1 kV. Since conventional coaxial DC blocks are not rated for these voltages, we created a DC block using two coaxial-waveguide adapters separated by a thin sheet of Teflon.

In order to work in the afterglow, a high voltage Insulated Gate Bipolar Transistor (IGBT), rated for 4.5 kV, switched off the discharge. As stated in the Introduction, the hairpin radiation is collected by a rectangular X-band waveguide onto a crystal detector. The following data was sent to the 4 channel LeCroy oscilloscope: discharge voltage, discharge current, frequency from the sweep generator and crystal detector signal.

4 C. Experimental results

Three hairpin resonance curves at 0.25 Torr are displayed in figure 12 (a) and three resonance curves at 0.75 Torr are displayed in figure 12 (b). With increasing current, the peak resonance frequency shifted to higher frequencies and the maximum signal decreased. The peak resonant frequency, f_{res}, with the discharge turned off is 3.079 GHz. Since the decrease in maximum signal is greater at higher pressure, we infer that electron-neutral collisions are causing the decrease. Spencer et al. [22] found similar absorption in microwave signal at pressures of 1 Torr or greater.

We calculated electron number densities using Eq. (5) with peak resonant frequencies derived from figure 13. Table I summarizes the information collected from the hairpin at both pressures for steady-state current values of 10 mA and 20 mA. Included in Table I are the reduced electric field (*E/N*), the electron number density determined with the numerical code, BOLSIG [13], the dimensionless quantities ω_p/ω & ν_{en}/ω, and the sheath correction factor. The *E/N* was determined by measuring the difference in floating potential of two wire probes separated axially by 2 cm in the positive column. The *E/N* and the current density were used as input parameters to BOLSIG. It should be noted that BOLSIG code calculation is more accurate

when the discharge *E/N* is less than 120 Td (Td = 10^{-17} V·cm^2.) In the active discharge at 0.25 Torr, the electron temperature was numerically estimated by BOLSIG to be 4.1 eV at 10 mA and 4.0 eV at 20 mA. In the active discharge at 0.75 Torr, the electron temperature was numerically estimated by BOLSIG to be 3.0 eV at 10 mA and 2.7 eV at 20 mA. These electron temperatures were used to solve for the electron Debye length and the sheath correction factor. In the four cases shown in Table I, the electron number densities measured by the hairpin resonator were in good agreement with the numerically-derived values.

In order to convert the hairpin resonator into a time-dependent diagnostic tool, resonance curves were built up at multiple points in time in the afterglow. This is informally known as the 'boxcar' approach and can be seen visually in Figure 13. An electron number density was determined at each point in time by measuring f_{res} and by converting f_{res} into an electron number density using Eq. (5). The decay of the electron number density in the afterglow is plotted in figure 7 at pressures of 0.25, 0.50 & 0.75 Torr. The data at 0.50 Torr is included in order to show the trend in the decay time and the trend in the initial electron number density for a constant current.

Both the electron Debye length and the electron-neutral collision frequency decrease in the first microsecond after switching off the discharge because the mean electron energy decreases [27]. The electron Debye length is constantly changing in the afterglow as the electron number density decreases with time. To account for the changing sheath correction factor, the electron Debye length and electron number density are solved iteratively at every point in time in the afterglow. As shown in figure 14, the decay of the electron number density is a straight line on a log-linear scale when the electron number density is above 2×10^8 cm^{-3}.

4 D. Analysis

The decay times measured in figure 14 were compared with theoretical values for the decay time due to ambipolar diffusion to the wall. Ambipolar diffusion holds when the characteristic length of diffusion is ten times greater the electron Debye length [28]. In the near afterglow (shown), the diffusion is ambipolar, but when the electron number density drops below 2×10^8 cm^{-3}, there is a transition to free electron diffusion (not shown). The ambipolar diffusion coefficient, D_a, increases with increasing pressure because the mobility of the positive ions decreases with increasing pressure. When the length of the discharge is much greater than the radius of the discharge, the loss of electrons to the wall via ambipolar diffusion is given by Raizer [24] as

$$\frac{\partial n_e}{\partial t} = -D_a \nabla^2 n_e$$
$$\text{where } \nabla^2 = \frac{1}{\Lambda^2} = \left(\frac{2.4}{R}\right)^2 \quad \text{and} \quad D_a = \mu_{ion}\frac{kT_e}{e} \qquad (10)$$

where Λ is the characteristic length of diffusion, R is the radius of the glass tube and kT_e/e is the electron temperature in Volts. The zero-field reduced mobility of N_2^+ in N_2 is $\mu_{ion} = \frac{1.87\times10^3}{p[Torr]}\frac{cm^2}{V\cdot\sec}$ [29]. The e-folding decay time of the electron number density, τ, is

$$\tau \approx \frac{e}{\mu_{ion} k T_e}\left(\frac{R}{2.4}\right)^2 = \frac{209 \times p[Torr]}{kT_e[eV]} \ [\mu s] \ \ for \ \ R = 1.5 \ cm \qquad . \qquad (11)$$

We now compare the theoretical decay times with the experimentally-derived decay times shown in figure 14. For the following analysis, we assume that there is no production of electrons in the afterglow via either direct electron impact ionization or Penning/associative ionization and we assume that the only loss of electrons is surface recombination at the wall via ambipolar diffusion. The last assumption is valid because, at this range of electron number densities and neutral gas pressure, the loss of electrons via volume processes, such as dissociative recombination or three body recombination, is significantly less than the loss via ambipolar diffusion to the wall [24]. At 0.25 Torr, 0.5 Torr and 0.75 Torr, the experimentally measured e-folding decay times were 110 μs, 190 μs and 250 μs, respectively. These decay times correspond to electron temperatures of 0.48 eV, 0.55 eV and 0.63 eV, respectively. At this range of pressures in nitrogen, the electron temperature can be kept far above the gas temperature by superelastic collisions with non-equilibrium electronic ground state vibrational species and with metastables, such as $A\ ^3\Sigma_u^+$.

The inferred electron temperatures are consistent with experimental and numerical data reported by Spencer et al. [22] and Guerra et al. [27]. At 1 Torr, Spencer et al. [22] indirectly measured an electron temperature of 0.6 eV in the afterglow using a microwave cavity resonator. At 3.3 Torr, Guerra et al. [27] calculated an electron temperature of 0.7 eV in the near afterglow (1 μs < t < 100 μs). We report indirect experimental evidence that the electron temperature in the nitrogen afterglow does not decay to the gas temperature (~0.05 eV), or to the vibrational temperature (~0.2 eV) [24]. Instead, the electron temperature in the near afterglow stays between 0.4 eV and 0.7 eV, depending on gas pressure.

4 E. Conclusion

A hairpin resonator was used to measure the electron number density in nitrogen glow discharges and in the afterglow. We addressed the effect of electron-neutral collision frequency when operating the hairpin at pressures near 1 Torr. By comparing measured steady-state results with numerical calculations, we demonstrated that the hairpin can accurately measure electron numbers density if an appropriate sheath correction factor is included. In order to measure a change in electron number density with time, we used a ‘boxcar’ approach by collecting data versus time in afterglow at a range of different microwave frequencies. We compared the measured decay of the electron number density to the theoretical decay by ambipolar diffusion to the wall and determined that the electron temperature in the near afterglow stays between 0.4 eV and 0.7 eV, depending on gas pressure. This confirms previous work by Spencer et al. [22] and Guerra et al. [27].

Table I: Experimental and Numerical Steady State Results

Pressure [Torr]	Current [mA]	E/N [Td]	Experimental Electron Number Density [cm-3]	Numerical Electron Number Density [cm-3]	Normalized Plasma Frequency [ ]	Normalized Collision Frequency [ ]	Sheath Correction Factor [ ]
0.25	10	160	6.2E+08	6.3E+08	0.07	0.05	0.76
0.25	20	155	1.2E+09	1.4E+09	0.10	0.05	0.83
0.75	10	124	9.0E+08	9.3E+08	0.09	0.15	0.83
0.75	20	115	2.0E+09	2.1E+09	0.13	0.15	0.89

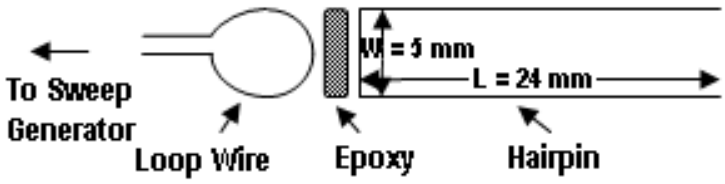

Figure 8. Diagram of Hairpin Resonator. W = hairpin width and L = hairpin length.

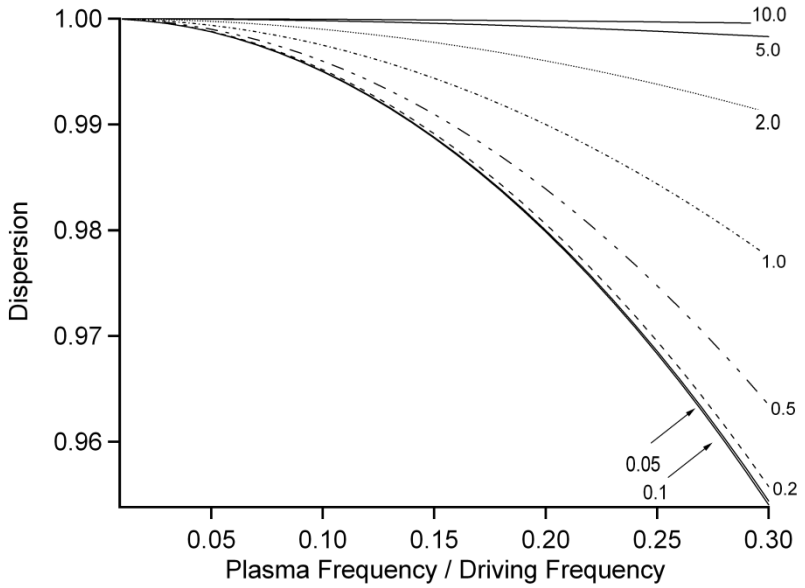

Figure 9. Real Part of the Square Root of the Dielectric Constant (dispersion) Versus Normalized Plasma Frequency (ω_p/ω) for a Range of Normalized Collision Frequencies (ν_{en}/ω)

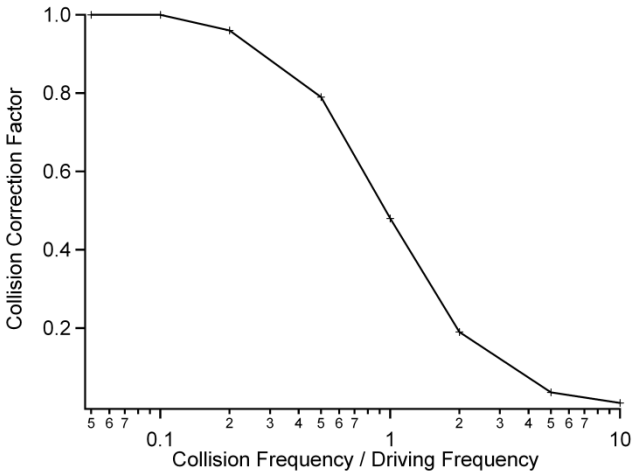

Figure10. Collision Correction Factor Versus Normalized Collision Frequency (ν_{en}/ω.)

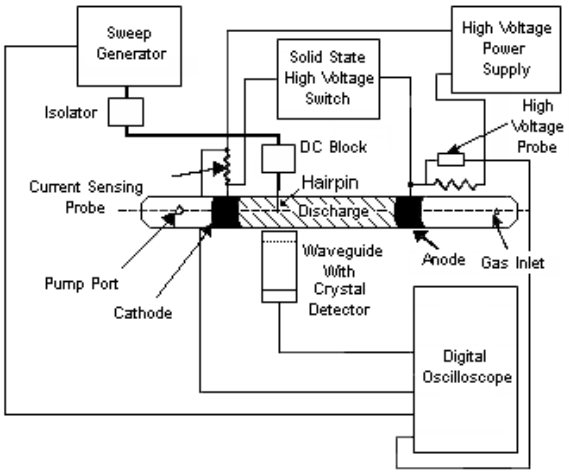

Figure 11. Schematic of the Experiment. See Experimental Setup Section for a More Detailed Explanation

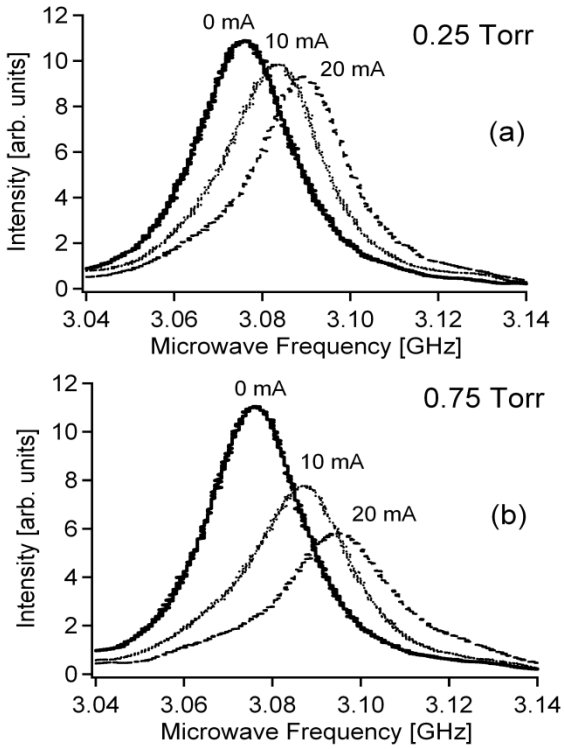

Figure 12 (a) Three Resonance Curves at 0.25 Torr. (b) Three Resonance Curves at 0.75 Torr.

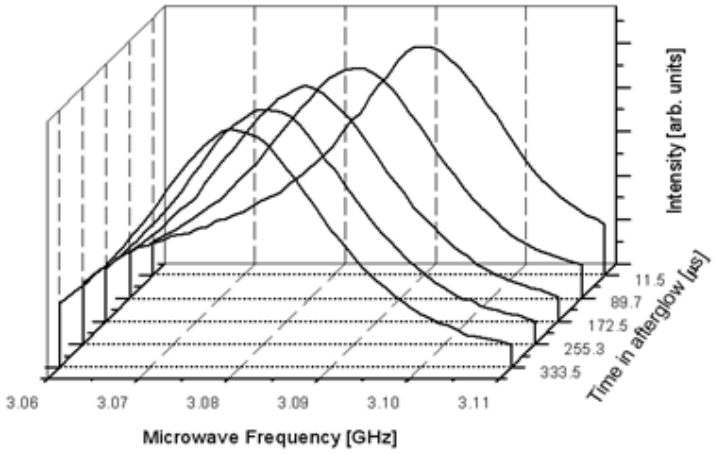

Figure 13. The Boxcar Approach for Time-dependent Electron Number Densities. Resonance Curves at Selected Points in Time in the Afterglow Are Shown at a Pressure of 0.25 Torr

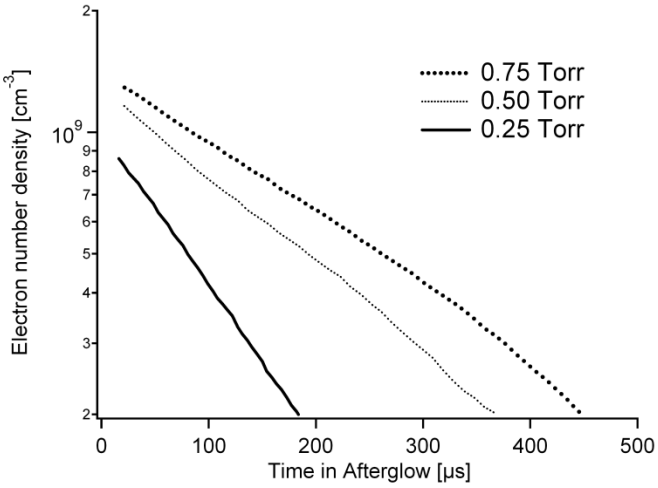

Figure14. Electron Number Density versus Time in the Nitrogen Afterglow. At Each Pressure, the Current before Switching Off the Discharge Was 15 mA

5. Effects of pulsed-excitation applied voltage rise time on argon metastable production efficiency in a high pressure dielectric barrier discharge

Many practical high pressure Dielectric Barrier Discharge (DBD) applications [30] require large electrode areas to achieve large surface area processing while maintaining high plasma-chemical and electrical efficiency. For example, ultraviolet (UV) and vacuum ultraviolet (VUV) radiation generated from large area lamps are used for mercury-free commercial lighting [30-35], large area (or volume) sterilization [30, 35, 36], and surface cleaning and modification [30, 38, 39].

Excitation of a DBD using fast rise-time, high voltage pulses are known to result in higher plasma-chemical efficiencies accompanied by a small average gas temperature rise as compared to those excited using an a.c. high voltage source [34,38-42] because the gap breakdown occurs at a higher overvolted condition [44], so the discharge operates at a higher E/n. This is evident (and illustrated below in figure 1) by the decreasing temporal delay between the displacement and the conduction current peaks as the applied voltage rise time is increased [43, 44]. The plasma-chemical reaction rates exponentially increase with increasing E/n [44, 45] which leads to higher plasma-chemical efficiency. The total instantaneous circuit current is given by [45]

$$I_{tot}(t) = \left(\frac{1}{1+\kappa}\right)\left(I_d(t) + C_g \frac{dV_{appl}}{dt}\right) \quad , \qquad (12)$$

where $I_d(t)$ is the discharge current, C_g, the gap capacitance, $\kappa = C_g / C_d$, C_d, the dielectric capacitance, and dV_{appl}/dt is the time rate of change of the total applied voltage. Equation 12 suggests that fast-pulse DBD excitation requires a minimization of C_g to increase the direct electron impact excitation efficiency, by minimizing the circuit power deposition through the displacement current [46]. For small DBD electrode structures having small κ and C_d, fast rise-time pulses at high E/n can be achieved, although the external circuitry can be somewhat complex and costly compared to a.c. excitation [30,38,40,46]. At high pressure, as the short-pulse excited DBD is scaled to large electrode area (for the same gap spacing, dielectric, and gas), the coupling between the external circuit, the discharge, and displacement currents cannot be ignored because the power supply must be able to provide the total instantaneous current and power to compensate for dielectric losses which are caused mostly through surface charging [30,40,46]. The implementation of short-pulse excitation at high pressures and large electrode areas becomes complex and costly for practical use because dielectric losses and non-linear parasitic electromagnetic effects scale with the surface area.

We have measured the effects of pulsed-excitation applied voltage rise-time on argon metastable (Ar^m) production efficiencies in a DBD operating at pressures between 100-500 Torr and with 1.6-6 kV total applied voltages, using two different unipolar high-voltage excitation pulses having rise times of ~10 ns (10%-90%) ("short-pulse") and ~150 ns ("long-pulse"). The impact of dielectric losses upon the Ar^m production efficiencies for both cases was assessed on the basis of energy deposition estimates using (i) the total circuit energies and (ii) only the discharge energies.

The DBD (3 × 1 × 0.5 cm, 1.5 mm thick Pyrex™ dielectric) was operated at 5 kHz repetition rate. Short-pulse operation and details of the current-voltage (I-V) measurements have been previously described in Ref. [46]. Long-pulse operation was achieved using a controlled

modification of the external circuit RC time constant. The instantaneous discharge currents were estimated from the difference between the measured total and displacement currents (the later was measured at pressures high enough to prevent a discharge [46]). Upper bound estimates of both the total and discharge energy depositions were performed by time integrating the product of the measured total applied voltage and the respective currents [40,46]. These are upper bound estimates (to within ~25%) because the total applied voltage (with respect to ground potential) is the sum of the voltages across the discharge and dielectric barrier.

In figures 15a and 15b we show I-V traces resulting from both short and long-pulse excitations obtained at 500 Torr with 6 kV total applied voltage, respectively. The total current prior to the onset of gas breakdown is due entirely to the displacement current, which was assessed as the difference between the total and discharge currents. In figure 15a, the short-pulse displacement current at the onset of breakdown is ~2 A, which is ~40 % of the ~5 A peak discharge conduction current. The long-pulse displacement current in figure 15b, peaking ~75 ns prior to breakdown, is ~10% of the ~2 A peak discharge current. For all pressure-voltage conditions, the long-pulse peak and average discharge currents were less than that of the short-pulse by ~50%. Compared to the short-pulse case, the temporal overlap of the long-pulse displacement and discharge currents were negligible, and the long-pulse upper bound energy deposition estimates were ~30-40 % lower, but exhibited similar pressure scaling. The indication that all long-pulse discharges were a "single-strike" was given by the agreement between the discharge current waveform shapes and volume averaged spontaneous emission at ~750 nm detected via a fiber-optic coupled photomultiplier tube and spectral band pass filter. Taken together, these results indicate that dielectric losses were mitigated by decreasing dV_{appl}/dt but at the expense of discharge energy deposition.

Spatially averaged, absolute $1s_3$ and $1s_5$ Ar^m column densities were measured using a single-pass Tunable Diode-Laser Absorption Spectroscopy (TDLAS) technique developed for pulsed operation, described in Ref [39]. Collision-broadened transmission profiles of both $1s_3 \rightarrow 2p_2$ (772.4207 nm) and $1s_5 \rightarrow 2p_7$ (772.376 nm) transitions [48], separated by ~22.5 GHz, were measured using a single wavelength scan. For the short-pulse case, the $1s_5 \rightarrow 2p_7$ absorption was maintained at $\approx 20 \pm 2\%$ by adjusting the total applied voltage and power at each pressure condition. Figure 16 compares two TDLAS scans for both long and short-pulse operation at 500 Torr with 6 kV total applied voltages. The simultaneously acquired 2 GHz Free-Spectral Range (FSR) étalon reference signal is shown at the bottom of the plot. The 100% transmission "baseline" was obtained by turning off the discharge. Qualitatively, these absorption spectra imply that the total Ar^m population generated by the short-pulse excitation is greater than that of the long-pulse.

Absolute Ar^m column densities (cm^{-2}) were obtained from the spectra using the Beer-Lambert absorption law and a narrowband laser approximation [48],

$$n_1 L = \frac{-c \ln(1-\alpha)}{h\nu_{o,a} B_{12} \varphi_a(\nu_{o,a})} \quad , \qquad (13)$$

where α is the absorption, B_{12} the Einstein absorption coefficient, $\varphi_a(\nu_{o,a})$ the area-normalized Voigt lineshape function evaluated at center absorption frequency $\nu_{o,a}$, h is Planck's constant, and c is the speed of light. The area-normalized lineshape functions were estimated with sufficient accuracy (10%) for p>50 Torr using Whiting's approximation [49] in the Lorentzian limit,

$$\varphi\left(\nu_{o,a}\right) \approx \frac{0.637}{w_V} \quad , \tag{14}$$

where w_V is the total Voigt-width component FWHM. For both transitions, the values of w_V were obtained to within ±10% uncertainty using multi-peak fitting commercial software.

Figure 17 shows the pressure scaling of absolute Ar^m column densities (cm^{-2}) obtained via equations (13) and (14) applied to the TDLAS spectra. Above 100 Torr, the Ar^m column densities generated by applying short-pulse excitation exceeded those obtained using the long-pulse, especially at 500 Torr.

Lower bound production efficiency estimates were computed from the ratio of the energy necessary to create a volume-averaged Ar^m population (via direct electron impact excitation) to the upper bound volume-averaged energy deposition estimates discussed above. The energies for creating the total Ar^m populations were estimated from the product of the measured total column densities, the electrode gap and length (transverse to the absorption path), and an average electron impact energy "cost" of 16 eV [50]. The pressure scaling of Ar^m production efficiency and the discharge energy deposition neglecting dielectric losses for both short and long pulse are plotted in figure 18. In figure 18, the long-pulse operation exhibited lower production efficiencies compared to those of the short-pulse under similar operating conditions, while in figure 18b, the long-pulse excitation efficiencies exhibit only a minor, uniform decrease over the entire pressure range. In this case, based on the total deposited energy, Ar^m production by the short-pulse dropped to the extent that the efficiency values and scaling for both cases are essentially the same within the experimental uncertainties. It should be noted that for each operating condition, the ratio of the discharge energy to the total energy was smaller for the long pulse than for the short pulse.

In conclusion, using the unipolar ~150 ns rise-time applied voltage pulse results in a slightly lower E/n discharge at high pressure as compared to short-pulse operation, inferred from both discharge energy, and absolute Ar^m column densities estimates. However, the production efficiencies with dielectric losses included *are essentially the same* as those of the ~10 ns fast-rise time excitation pulse. These results indicate that a tradeoff exists between these two excitation schemes, and their use should be dictated by the chosen application.

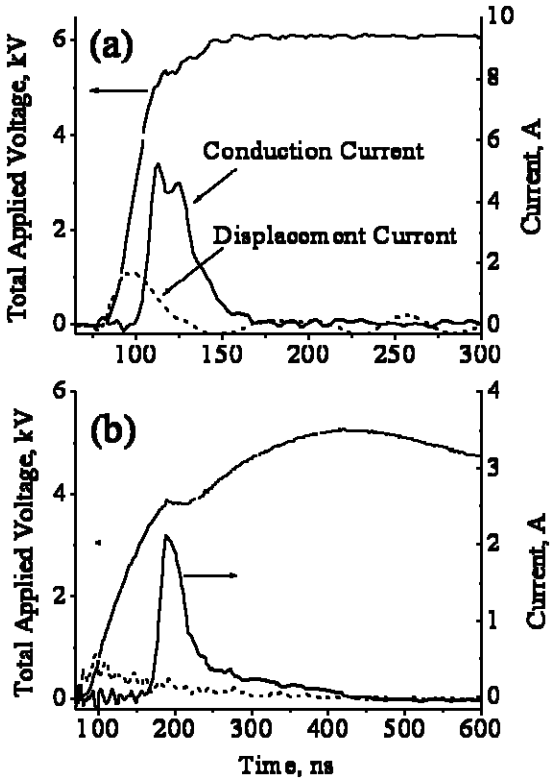

Figure 15. Voltage and Current Waveforms at 500 Torr, 6 kV Peak Applied Voltage, 5 kHz Pulse Repetition Rate using (a) 10 ns Rise-time Excitation Pulse (b) ~150 ns Rise-time Excitation Pulse

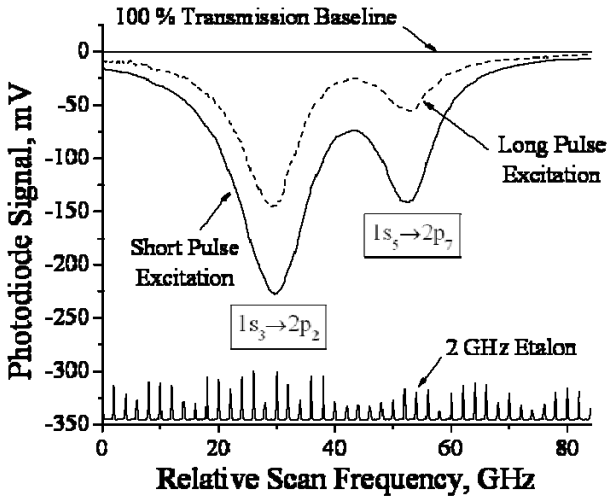

Figure 16. Absorption Scan of Both $1s_3 \rightarrow 2p_2$ and $1s_5 \rightarrow 2p_7$ Ar Transitions in Both Short-pulse and Long-pulse DBD at 500 Torr, 6 kV Peak Applied Voltage, 5 kHz Repetition Rate

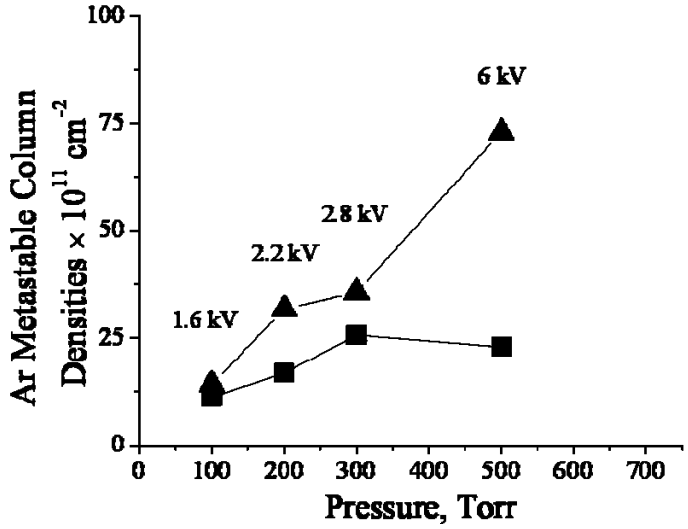

Figure 17. Measured Argon Metastable Column Densities as a Function of Pressure using Both Short-pulse and Long-pulse Excitation Schemes at 5 kHz Pulse Repetition Rate

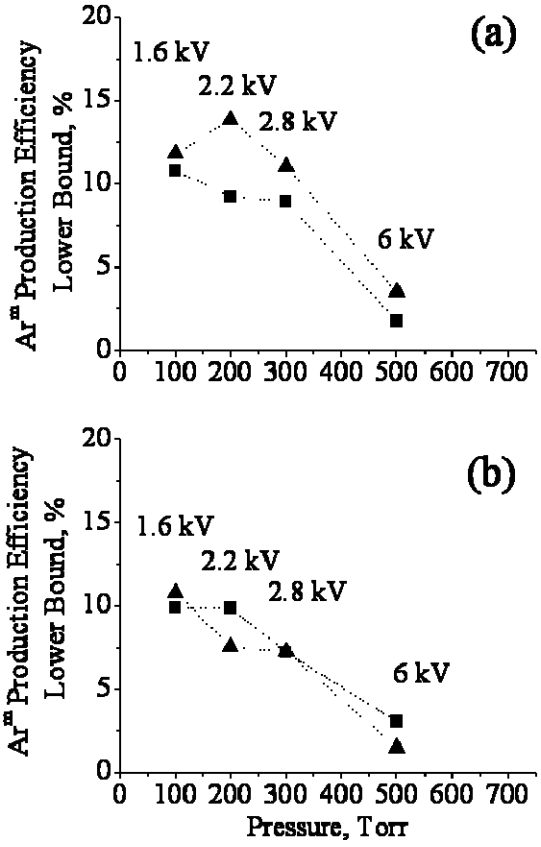

Figure 18. Lower Bound Argon Metastable Production Efficiency Estimates as a Function of Pressure for Both Short and Long Pulse Excitation Schemes

6. Properties and dynamics of a streamer-like dielectric capillary atmospheric pressure plasma jet

The atmospheric pressure plasma jet (APPJ) has been studied as a source for generating nonequilibrium atmospheric pressure plasmas for a variety of material processing and biomedical applications. Several APPJ devices have been studied including single-cell designs and multicell arrays. The APPJ source described in this letter is a single-cell dielectric capillary configuration. This source is formed from a dielectric capillary of a few millimeters diameter with electrodes surrounding it. This configuration was introduced by Teschke et al.[51] and has been subsequently studied in various forms [52,53] and as part of an array device.[54] It is typically excited using kV-range RF or pulsed power supplies at kHz repetition rates. In contrast to some other APPJ sources, this plasma jet is operated at lower gas flow rates and appears to be electrically driven.[51,52] Time-resolved imagery has shown that the jet is not a continuous volume of plasma, rather, it is composed of well defined propagating ionization fronts initially termed as ``plasma bullets.[1]" These plasma bullets are launched with the rising edge of the voltage cycle and propagate with speeds several orders of magnitude greater than the flow speed.[51,52] Lu and Laroussi [52] later proposed a streamer discharge model to explain the properties of these so called plasma bullets. In this letter, we show that the plasma jet formed outside this dielectric capillary configuration is electrically driven and is not directly coupled to the initiation of a dielectric barrier discharge within the capillary. The temporal development and structure of this plasma jet is similar to that of a self-sustained streamer discharge in free space. This differs from other APPJ sources that exist as a flow-driven effluent sustained from an upstream discharge.

Figure 19 shows our dielectric capillary experimental configuration. A gas mixture of primarily He with a variable Ar concentration was flowed through a cylindrical glass capillary with a 2 mm i.d. and a 3 mm o.d. Copper ring electrodes surrounded the capillary. The anode ring was placed near the end of the capillary and was separated from the cathode ring by ~1 cm. When energized, a capillary dielectric barrier discharge (CDBD) is excited inside this gap with a plasma jet extending beyond the edge of the capillary (cf. Fig.25). The plasma jet was terminated through a virtual ground plane as no physical electrode was present beyond the capillary. We excited the discharge using a positive-going unipolar voltage pulse with a rise time of 20 ns. Table II lists the ranges of other electrical parameters and ranges for the gas flow rates and mixture ratios that were studied. The most notable difference between this setup and others in the literature is the faster rise time of the voltage pulse. We will discuss the possible impact of this on our results.

TABLE II: Operating conditions for our dielectric capillary configuration. Conditions used for acquiring the data shown in Figs. 20-22 are listed in parentheses.

applied voltage	10-13 (11) kV
pulse repetition rate	0.6-3.0 (1.0) kHz
total gas flow rate	1.5-9.0 (4.5) standard l/m
Ar/He flow ratios	<1% - 25% (5%)

Wide bandwidth voltage and current probes were used to monitor the electrical properties. Plasma emission was monitored using two separate fiber-coupled photomultiplier tubes (PMTs). The detector monitoring the CDBD was stationary throughout the experiment while the plasma

jet detector could be translated between 2 and 34 mm from the edge of the capillary. The measured displacement current peak served as a timing reference for measuring the relative delay of the emission intensity peaks. The primary errors in determining the emission delay were due to the repeatability of the PMT response and the spatial resolution of the detector (~1 mm) and amounted to an error of ±2 ns. An intensified charge-coupled device (ICCD) camera with a 5 ns gate width was additionally used to monitor the CDBD and plasma jet. We used 10-nm band-pass filters centered at 340 nm, 390 nm, and 750 nm, respectively passing 337 nm emission from N_2 $C^3\Pi_u$-$B^3\Pi_g$ (0,0), 391.4 nm emission from N_2^+ $B^2\Sigma_u$-$X^2\Sigma_g$ (0,0) and 388.9 nm emission from the He 3^3P-2^3S metastable transition, and 750.4 nm emission from the Ar $3p^5 4p$-$3p^5 4s$ transition to complement unfiltered broadband measurements. The discharge conditions used to acquire the data in the following figures are listed in parentheses in Table I. Figure 20(a) shows a sequence of unfiltered images of the CDBD and plasma jet taken with the ICCD camera at 20 ns intervals from the onset of emission. The frames from each of the image sequences were integrated over 100 pulses to acquire sufficient signal to noise. The high degree of shot to shot repeatability, which is characteristic of this APPJ,[51-53] made this image integration possible. The noteworthy feature of Fig. 20(a) is the initiation of the plasma jet *before* the CDBD. This shows that the plasma jet is initiated independent of the discharge inside the capillary and indicates that the jet is a self-sustained discharge that is not directly coupled to the interior discharge. Figure 20(b) illustrates this more precisely with high intensity emission profiles from the 750 nm Ar transition averaged over 500 pulses acquired with the plasma jet (dashed line) and CDBD (dotted line) PMT detectors. The average total current (solid line) is also shown. The plasma jet detector was focused at ~2 mm beyond the edge of the capillary to ensure the capillary did not interfere in the measurement. The plasma jet emission at this location consistently led the inner discharge by 5-20 ns over the range of conditions listed in Table II, except for some conditions near the extremes of these ranges where the CDBD and plasma jet were marginally stable. Figure 20(b) represents a typical case with the interior discharge emission lagging by ~10 ns.

The additional ICCD image sequences in Figs. 21(a) and (b) show emission bands centered at 390 nm and 340 nm respectively and illustrate the temporal development and basic structure of the plasma jet. The frames in these sequences were integrated over 600 pulses due to the weaker emission from these bands. More detailed image sequences under the same conditions can be found in Ref. 55. Figure 21(a) tracks the leading ionization front via emission from N_2^+ and excited He and shows it to have a well-defined structure. Conversely, emission from the comparatively lower energy N_2 $C^3\Pi_u$ state in Fig. 21(b) shows the presence of a weakly-ionized plasma channel that can be seen persisting in the wake of the advancing ionization front, establishing current continuity with the anode. These properties are consistent with those of cathode-directed streamers in positive corona discharges.[56,57]

Figure 22 tracks the propagation of the ionization front using the filter centered at 390 nm. The ionization front propagates with a constant velocity over much of the ~3.5 cm length of the jet, with an apparent deceleration near the outer edge. The increasing error bars toward the outer edge resulted from a rapidly decreasing signal to noise and temporal fluctuations caused by ambient air currents that tended to broaden the 500-pulse averaged emission profile. The constant propagation velocity was consistent over the range of conditions studied. The propagation speed derived from the linear fit in Fig. 22 was $5.54 \pm 0.03 \cdot 10^7$ cm/s. Over the range of parameter space in Table II the measured speeds varied in a range of ~$4\text{-}8 \cdot 10^7$ cm/s and are consistent with previous results.[51,52] The dynamics of the ionization front also closely resemble the dynamics of cathode-directed streamers in a nonuniform field predicted with

numerical modeling[7,8] and observed experimentally in positive corona discharges.[59-61] Additionally, Morrow and Lowke [57] showed that a cathode-directed streamer propagating into free space will terminate once it has propagated to the point where current continuity between itself and the anode can no longer be maintained. This is characterized by a sharp decrease in the streamer electric field and rapid deceleration of the streamer as the photoionization sustaining its propagation is halted. This resembles our configuration without an external ground plane and it can explain the terminal behavior in Fig. 22. The data shown in Figs. 20-22 depict a very different APPJ source that does not rely on the transport of reactive species from the CDBD in order to form the jet outside the dielectric capillary. Instead, this electrically-driven APPJ has properties consistent with a cathode-directed streamer discharge in free space.

There are some notable differences between the streamer-like APPJ source described here and positive corona discharges that are typically used to study cathode-directed streamers. In a typical corona discharge, the electric field diverges outward in a wide angle from the anode and is guided by the presence of a nearby ground plane. This electric field in turn guides the streamers, which can develop along several paths with perhaps multiple bifurcations depending on conditions. Thus, streamer propagation is dependent on the shape of the electric field.[62,63] Streamers developed in pulsed positive corona discharges are typically not very repeatable due to the stochastic nature of their initiation and relatively wide area through which they can propagate. The streamers associated with this configuration are, in contrast, very repeatable and highly directed, tracing the same path consistently. In addition to the presence of a straight flow-gas channel outside the capillary, we also attribute this behavior to the focusing of the electric field along the capillary axis from cylindrically symmetric charge accumulation near the capillary tip during the rising edge of the unipolar voltage pulse, as indicated by the large displacement current in Fig. 20(b). We believe the short 20 ns risetime of the applied voltage pulse may have led to an increased surface charge accumulation that increased the local E/n and decreased the streamer initiation delay, thus enabling us to observe the plasma jet before the interior CDBD. In fact, the plasma jet is particularly sensitive to the capillary tip geometry, which would affect the magnitude and distribution of surface charge. Because it is a challenge to isolate specific streamers in a repeatable fashion in typical corona setups, [64] this APPJ source may be useful as a controlled experiment for the study of streamer discharges.

The results of this experiment show that the atmospheric pressure plasma jet, in this dielectric capillary configuration, is initiated *before* the interior CDBD This indicates that this plasma jet is a self-sustained discharge and not the flow-driven plasma effluent of the CDBD. This discharge has streamer-like properties. This corroborates the streamer discharge mechanism proposed to explain the rapidly propagating ionization fronts that make up the plasma jet.[52] An important distinction is that the APPJ described here can generate reactive species *in situ* at relatively large distances from the source (~3.5 cm under our conditions) rather than generating the reactive species remotely and transporting them downstream via the plasma effluent, as is the case with some other APPJ sources. This may be particularly useful for plasma chemical processing and other applications.

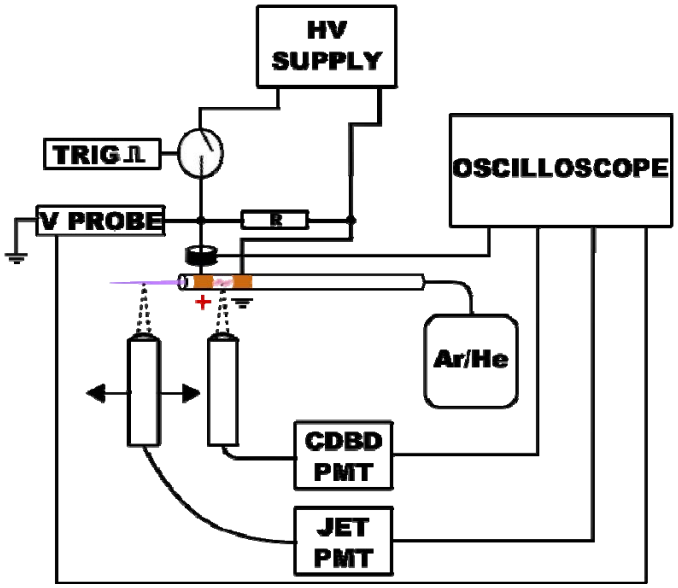

Figure 19. Diagram of the Experimental Apparatus and the Diagnostics Used for Studying this APPJ Source

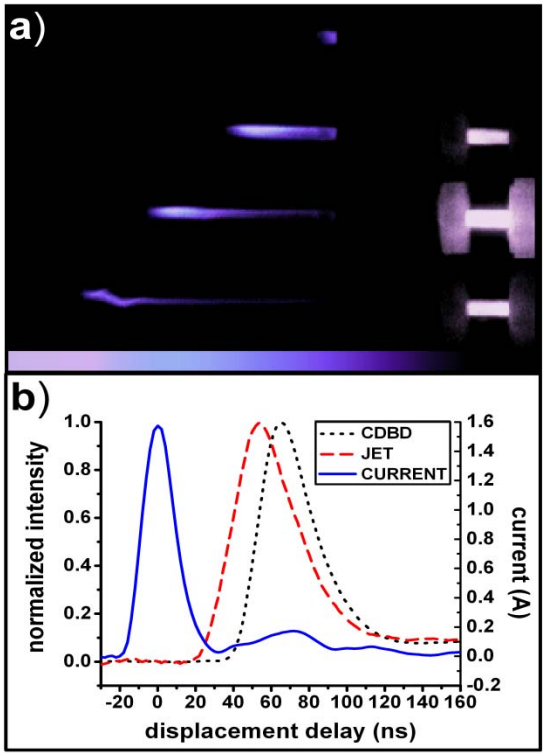

Figure 20. (a) Unfiltered Image Sequences of the Plasma Jet and CDBD Emission Acquired with a 5 ns Gated ICCD Camera. (b) Normalized Intensity from Displacement Current Delay

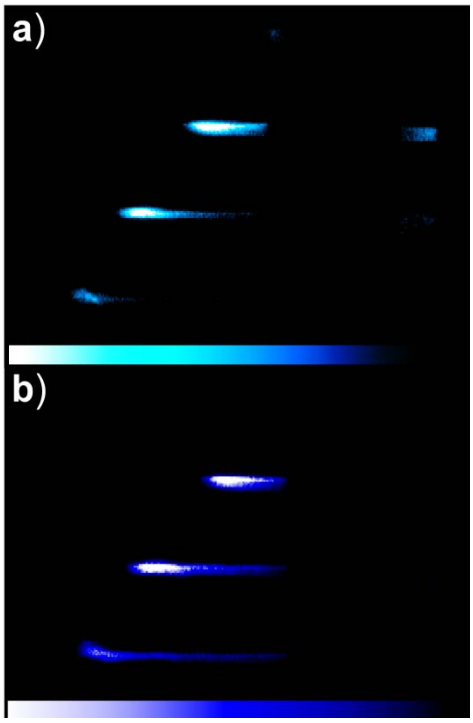

Figure.21. Image Sequences Acquired with an ICCD Camera Under the Same Conditions as Figure 20. The Images Show Emission Through 10-nm Band-pass Filters Centered at (a) 390 nm and (b) 340 nm

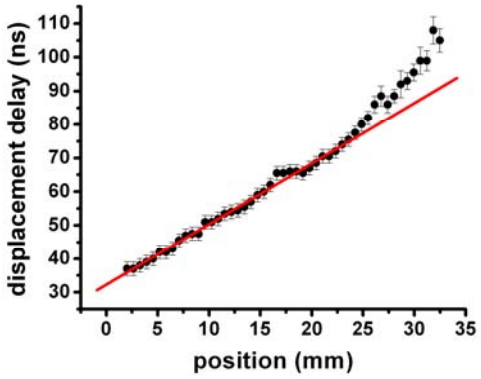

Fig. 22: Variation in arrival delay of the plasma jet emission with PMT detector position, measured with respect to the peak of the displacement current.

References

1. K. T. Rie, E. Menthe and J. Woehle, Surface and Coating Technol. 98, pp. 1192-1198, (1998).
2. M. S. Brown and B. N. Ganguly, AIAA Paper No. 03-0702 presented at 41st AIAA Aerospace Sciences Meeting and Exhibit, Reno, NV, 2002
3. T.C. Wagner, W.F. O'Brien, G.B. Northam and J.M. Eggers, J. Propulsion 5, 548 (1989)
4. T. Mitani, Combust. Flame 101, 347 (1995).
5. K. Khodataev and A. Ershov, in 2nd Weakly Ionized Gases Workshop, Proceedings Supplement, Norfolk, VA, p. 341-350, (1998).
6. Y. Y. Buriko, V. A. Vinogradov, V. A. Goltsev, and P. J. Waltrup, J. Propulsion and Power 18, 1049 (2002).
7. R. Dorai, K. Hassouni, and M. J. Kushner, J. Appl. Phys 88, 6060 (2000).
8. V. Puchkarev and M. Gundersen, Appl. Phys. Lett. 71, 3364 (1997).
9. R. S. Sigmond and M. Goldman in Electrical breakdown and discharges in gases eds.E.E. Kundhart and L. H. Luessen, Plenum, New York, 1981, pp 1-64.
10. S. D. Marcum, J. W. Parish, and B. N. Ganguly, J. Propulsion and Power 20, 360 (2004).
11. K. Niemi, V.S. von der Gathen, and H. F. Dobele, J. Phys. D: Appl. Phys. 34 2330 (2001).
12. A. von Engel, Ionized Gases, American Institute of Physics, New York, 1995, pp 222-236.
13. R. K. Janev, and D. Reiter, Phys. Plasmas 9, 4071 (2002).
14. R.L. Stenzel, Rev. Sci. Instrum. **47**, 603 (1976).
15. G.A. Hebner and A.C. Abraham, J. Appl. Phys. **90**, 4929 (2001).
16. R.B. Piejak, V. A. Godyak, R. Garner and B.M. Alexandrovich, J. Appl. Phys. **95**, 3785 (2004).
17. R.B. Piejak, J. Al-Kuzee and N. St. J. Braithwaite, Plasma Sources Sci. Technol. **14**, 734 (2005).
18. F.A. Haas, J. Al-Kuzee and N. St. J. Braithwaite, Appl. Phys. Lett., **87**, 201503 (2005).
19. O. Aucreillo and D.L. Flamm, *Plasma Diagnostics: Volume 1* (Academic Press, New York, 1989).
20. R.H. Huddlestone and S.L. Leonard, *Plasma Diagnostic Techniques* (Academic Press, New York, 1965).
21. M.A. Herald and C.B. Wharton, *Plasma Diagnostics with Microwaves* (John Wiley & Sons Inc., New York, 1965) pp. 6, 63-65.
22. Spencer, M.N., Dickinson, J.S. and Eckstrom, D.J., J. Phys. D **20**, 923 (1987).
23. K. Behringer and U. Fantz, J. Phys. D **27**, 2188 (1994).
24. Y.P. Raizer, *Gas Discharge Physics* (Springer-Verlag, Berlin, 1991), pp. 10, 28-29, 60-67, 204.
25. T.E. Sheridan and J. Goree, Phys. Fluids B **3**, 2796 (1991).
26. SIGLO Homepage. www.siglo-kinema.com/**bolsig**.htm
27. V. Guerra, F.M. Dias, J. Loureiro, P.A. Sá, P. Supiot, C. Dupret and T. Popov, IEEE Trans. Plama Sci **31**, 542 (2003).
28. Phelps, A.V., J. Res. Natl. Inst. Stand. Technol., **95**, 407 (1990).
29. Moseley, J.T., Snuggs, R.M., Martin, D.W. and McDaniel, E.W., Phys. Rev. **178**, 240 (1969).

30. U. Kogelshatz, Plasma Chem. and Plasma Processing **23**, 1 (2003).
31. N. Masoud, K. Martus, K. Becker, J. Phys. D: Appl. Phys. **38**, 1674 (2005).
32. H.B. Park, S.E. Lee, G.Y. Kim, Y.D. Lee, K.C. Choi, J. Disp. Tech. **2**, 60 (2006).
33. M. Jinno, H. Kurokawa, M. Aono, Jpn. J. Appl. Phys. **38**, Pt. 1, No. 7B, 4613 (1999).
34. R.J. Carman, I.S. Falconer, R.P. Mildren, IEEE Trans. Plasma Sci. **33**, 330 (2005).
35. Z.Falkenstein,Ushio America, Inc., http://www.ushiotpd.com/dmimages/IUVApaper.pdf (2001).
36. M. Heise, W. Neff, O. Franken, P. Muranyi, J. Wunderlich, Plasmas and Poly. **9**, 23 (2004).
37. S.J. Scott, C.C. Figgures, D.G. Dixon, Plasma Sources Sci. Technol. **13**, 461 (2004).
38. K. Okazaki, T. Nozaki, Pure Appl. Chem. **74**, 447 (2002).
39. 10. R.J. Leiweke, B.N. Ganguly, Appl. Phys. Lett. **88**, 131501 (2006).
40. J.M. Williamson, D.D. Trump, P. Bletzinger, B.N. Ganguly, J. Phys. D: Appl. Phys. **39**, 4440 (2006).
41. R.P. Mildren, R.J. Carman, I.S. Falconer, IEEE Trans. Plasma Sci. **30**, 192 (2002).
42. R.P. Mildren, R.J. Carman, J. Phys. D: Appl. Phys. **34**, L1 (2001).
43. Korolev, Yu.D., Mesyats, G.A., "Physics of Pulsed Breakdown in Gases", URO Press, Moscow, Russia, (1998), pp 151-153.
44. 15. A. von Engel, "Ionizes gases", American Institute of Physics, Woodbury, New York, 1994, pp 180- 215.
45. 16. S. Liu, M. Neiger, J. Phys. D: Appl. Phys. **36**, 3144 (2003).
46. 17. P. Bletzinger, B.N. Ganguly, J. Phys. D: Appl. Phys. **36**, 1550 (2003).
47. 18. National Institute of Standards and Technology Atomic Spectra Database, v3.1.0 http://physics.nist.gov/PhysRefData/ASD/index.html
48. 19. W. Demtröder, "Laser Spectroscopy", 2nd Edition, Springer-Verlag, New York, pp. 367-372 (1998).
49. 20. E.E. Whiting, J. Quant. Spectrosc. Radiat. Transfer 8, 1379 (1968).
50. 21. R.S. Schappe, M.B. Schulman, L.W. Anderson, and C.C. Lin, Phys. Rev. A **50**, 444 (1994).
51. M. Teschke, J. Kedzierski, E. G. Finantu-Dinu, D. Korzec, and J. Engemann, IEEE Trans. Plasma Sci. 33, 310 (2005).
52. X. Lu and M. Laroussi, J. Appl. Phys. 100, 063302 (2006).
53. O. Sakai, Y. Kishimoto, and K. Tachibana, J. Phys. D: Appl. Phys. 38, 431 (2005).
54. J. L. Walsh, J. J. Shi, and M. G. Kong, Appl. Phys. Lett. 88, 171501 (2006).
55. B. Sands, B. Ganguly, and K. Tachibana, IEEE Trans. Plasma Sci. (2008), (in press).
56. R. Morrow and J. Lowke, J. Phys. D: Appl. Phys. 30, 614 (1997).
57. S. Pancheshnyi, M. Nudnova, and A. Starikovskii, Phys. Rev. E. 71, 16407 (2005).
58. S. Dhali and P. Williams, J. Appl. Phys. 62, 4696 (1987)
59. F. Grange, N. Soulem, J. Loiseau, and N. Spyrou, J. Phys. D: Appl. Phys. 28, 1619 (1995).
60. A. Kulikovsky, IEEE Trans. Plasma Sci. 25, 439 (1997).
61. W. Yi and P. Williams, J. Phys. D: Appl. Phys. 35, 205 (2002).
62. E. van Veldhuizen and W. Rutgers, J. Phys. D: Appl. Phys. 35, 2169 (2002).
63. E. van Veldhuizen, A. Baede, D. Hayashi, and W. Rutgers, APP Spring Meeting (Bad Honnef, Germany, February 2001) pp. 231-4 (2001).
64. R. Tardiveau, E. Marode, and A. Agneray, J. Phys. D: Appl. Phys. 35, 2823 (2002).

7. Publication list

Book chapter:

B.N. Ganguly, W.R. Lempert, K. Akhtar, J.E. Scharer, F. Leipold, C.O. Laux, R.N. Zare, and A.P. Yalin, "Plasma Diagnostics" in Nonequilibrium Air Plasmas at Atmosphere Pressure, (Institute of Physics, Bristol, UK 2005)

Review Article:

P. Bletzinger, B. N. Ganguly, D. Van Wie and A. Garscadden, "Plasmas in high speed aerodynamics", J. Phys D.: Appl. Phys.38, R33 (2005)

Publications:

D. L. Wisman and B. N. Ganguly, "Point to plane corona discharge for high speed reacting flow visualization", Expts. In Fluids (to be published)

B. L. Sands, R. J. Leiweke, B. N. Ganguly, "Spatiotemporally resolved Ar ($1s_5$) metastable measurements in a streamer-like He/Ar atmospheric pressure plasma jet", J. Phys.D: Appl. Phys.43, 282001 (2010)

F. Liu, G. Huang, B. Ganguly, "Plasma excitation dependence on voltage slew rates in 10-200 Torr argon-nitrogen gas mixture DBD", Plasma Sources Sci Technol 19, 045017 (2010)

K. Urabe, T. Morita, K. Tachibana and B. Ganguly, "Investigation of discharge mechanisms in helium plasma jet at atmospheric pressure by laser spectroscopic measurements", J. Phys. D: Appl. Phys 43, 095201 (2010)

C.Q. Jiao, B. N. Ganguly and A. Garscadden, "Mass spectrometry study of decomposition of JP-10 by low-power, low-pressure rf plasma", J. Appl. Phys. 105, 033305 (2009)

B.L Sands, S.K. Huang and B. N. Ganguly, "Current scaling in an atmospheric pressure capillary dielectric barrier discharge", Appl. Phys. Lett. 95, 051502 (2009)

D. L. Wisman, S. D. Marcum, B. N. Ganguly, "Chemi-ion current induced dissociative recombination in premixed hydrocarbon/air flames", Journal of Propulsion & Power 24, 1079 (2008)

D. L. Wisman, B. N. Ganguly, S. D. Marcum, "High-speed visualization of flame reaction zone using a positive point-to-plane corona discharge", IEEE Trans. Plasma Science, 36, 928 (2008)

K. Urabe, Y. Ito, K. Tachibana and B. Ganguly, "Behavior of N_2^+ ions in He microplasma jet at atmospheric pressure measured by laser induced fluorescence spectroscopy", Appl. Phys. Express 1, 066004 (2008)

B. L. Sands, B. N. Ganguly and K. Tachibana, "A streamer-like atmospheric pressure plasma jet, Appl. Phys. Lett., 92, 151503 (2008)

C. Jiao, A. Garscadden, and B. Ganguly, "Charge transfer reaction in Xe plasma expansion", J. Appl. Phys. 101, 083308 (2007)

B. N. Ganguly, "Hydrocarbon combustion enhancement by applied electric field and plasma kinetics", Plasma Phys. Control Fusion 49, B239 (2007)

D. L. Wisman, S. D. Marcum, B. N. Ganguly, “Electrical control of the thermodiffusive instability in premixed propane-air flames”, Combust. Flame 151, 639 (2007)

J. M. Williamson, D.D. Trump, P. Bletzinger, and B. N. Ganguly, “Comparison of high voltage ac and pulsed operation of a surface dielectric barrier discharge”, J. Phys D: Appl. Phys. 39, 4400 (2006)

R.J. Leiweke and B. N. Ganguly, “Temperature measurement in a high pressure dielectric barrier discharge using pressure induced line broadening and frequency shift”, Appl. Phys. Lett. 88, 131501 (2006)

N. S. Siefert, B.N. Ganguly, B. L. Sands, and G. A. Hebner, “Decay of electron number density in the nitrogen afterglow using hairpin resonator probe”, J. Appl. Phys 100, 043303 (2006)

N. Siefert, B. N. Ganguly, and P. Bletzinger, “Shock wave induced enhancement of optical emission in nitrogen afterglow plasma”, Phys. Rev.E 72, 066402 (2005)

P. Bletzinger, B. N. Ganguly and A. Garscadden, “Influence of dielectric barrier discharges on low Mach number shock waves at low to medium pressures”, J. Appl. Phys. 97, 113303 (2005)

S. D. Marcum and B. N. Ganguly, “Electric field induced flame speed modification”, Combust and Flame 143, 27 (2005)

J. M. Williamson, P. Bletzinger and B. N. Ganguly, “Absolute and relative density measurements in a N_2/Ar dielectric barrier discharge by diode-laser absorption spectroscopy and resolved plasma emission”, J. Appl. Phys. 97, 103301 (2005)

M. S. Brown, R. A. Forlines, and B. N. Ganguly, “Measurement of CH density in a pulsed-dc hydrocarbon gas mixture discharge”, J. Appl. Phys. 97, 103302 (2005)

M. S. Brown, R. A. Forlines, and B. N. Ganguly, “Streamer evolution in a methane-based pulsed dc discharge”, IEEE Transaction on Plasma Science 33, 256(2005)

P. Bletzinger, B. N. Ganguly, and A. Garscadden, "Effect of shock wave propagation on plasma emission in a low pressure N_2 discharge", IEEE Transaction on Plasma Science 33, 342 (2005)

J. M. Williamson, P. Bletzinger and B. N. Ganguly, “Gas temperature determination in aN_2/Ar dielectric barrier discharge by diode-laser absorption spectroscopy and resolved plasma emission”, J. Phys. D: Appl. Phys. 37, 1658 (2004)

S. D. Marcum, J. W. Parish and B. N. Ganguly, “Methane Dissociation in Pulsed DC Discharges at High Reduced Electric Field”, J. Propulsion and Power 20, 304 (2004)

B. N. Ganguly and J. W. Parish, “Absolute H atom density measurement in a pure methane pulsed discharge,” Appl. Phys. Lett. 84, 4953 (2004)